

Probing biological nanotopology via diffusion of weakly constrained plasmonic nanorods with optical coherence tomography

Raghav K. Chhetri^{a,1}, Richard L. Blackmon^a, Wei-Chen Wu^b, David B. Hill^{a,c}, Brian Button^c, Patricia Casbas-Hernandez^d, Melissa A. Troester^d, Joseph B. Tracy^b, and Amy L. Oldenburg^{a,e,2}

^aDepartment of Physics and Astronomy, University of North Carolina at Chapel Hill, Chapel Hill, NC 27599-3255; ^bDepartment of Materials Science and Engineering, North Carolina State University, Raleigh, NC 27695; ^cCystic Fibrosis/Pulmonary Research and Treatment Center, University of North Carolina at Chapel Hill, Chapel Hill, NC 27599-7248; ^dLineberger Comprehensive Cancer Center/Department of Epidemiology, University of North Carolina at Chapel Hill, Chapel Hill, NC 27599-7295; and ^eBiomedical Research Imaging Center, University of North Carolina at Chapel Hill, Chapel Hill, NC 27599-7513

Edited by Changhui Yang, California Institute of Technology, Pasadena, CA, and accepted by the Editorial Board September 3, 2014 (received for review May 19, 2014)

Biological materials exhibit complex nanotopology, i.e., a composite liquid and solid phase structure that is heterogeneous on the nanoscale. The diffusion of nanoparticles in nanotopological environments can elucidate biophysical changes associated with pathogenesis and disease progression. However, there is a lack of methods that characterize nanoprobe diffusion and translate easily to in vivo studies. Here, we demonstrate a method based on optical coherence tomography (OCT) to depth-resolve diffusion of plasmon-resonant gold nanorods (GNRs) that are weakly constrained by the biological tissue. By using GNRs that are on the size scale of the polymeric mesh, their Brownian motion is minimally hindered by intermittent collisions with local macromolecules. OCT depth-resolves the particle-averaged translational diffusion coefficient (D_T) of GNRs within each coherence volume, which is separable from the nonequilibrium motile activities of cells based on the unique polarized light-scattering properties of GNRs. We show how this enables minimally invasive imaging and monitoring of nanotopological changes in a variety of biological models, including extracellular matrix (ECM) remodeling as relevant to carcinogenesis, and dehydration of pulmonary mucus as relevant to cystic fibrosis. In 3D ECM models, D_T of GNRs decreases with both increasing collagen concentration and cell density. Similarly, D_T of GNRs is sensitive to human bronchial-epithelial mucus concentration over a physiologically relevant range. This novel method comprises a broad-based platform for studying heterogeneous nanotopology, as distinct from bulk viscoelasticity, in biological milieu.

dynamic light scattering | plasmon resonance | nanoparticle diffusion | diffusion in mucus | diffusion in extracellular matrix

Biological fluids (e.g., blood, mucus, saliva, synovial fluids) and soft solids [e.g., collagen, extracellular matrix (ECM), cytoskeleton] consist of a milieu of small molecules (making up the solvent) and large molecules (proteins and polymers making up the mesh or matrix) that are collectively responsible for their viscoelastic nature. Traditional rheological methods characterize the bulk viscoelastic properties of such biological media. However, nanoscopic objects, such as viruses and drugs that are smaller than the polymeric correlation length of the biological tissue network, encounter mechanical environments that are entirely different from that described by bulk viscoelasticity. For instance, at the nanoscale, mucus is a heterogeneous network of mucin fibers, nonmucin proteins, cell debris, lipids, DNA, actin filaments, and salts in a low-viscosity interstitial fluid (1). Similarly, tissue ECM, although soft solid-like in bulk, is an interconnected mesh of elongated protein fibers riddled with pores that are filled with low-viscosity interstitial fluids.

Microrheological techniques based on the generalized Stokes–Einstein relation (2–5) are capable of converting the observed diffusion of probes of controlled hydrodynamic size into a mea-

sure of the frequency-dependent viscoelasticity. Similarly, the use of optical tweezers constitutes an active rheology method that has been used to describe mucus (6) and cancer cell (7) viscoelastic properties. However, such techniques typically use micrometer-scale spheres as rheological probes and, thus, do not elucidate nanoscale rheology encountered in weakly constraining biological environments. Noninvasive measurement of nanoprobe diffusion in complex biological environments is outside the capability of a majority of current rheological techniques due to a lack of imaging penetration depth and/or the diffraction limit of the optical microscope. To access the frontier of nanoscale biorheology, techniques that characterize the diffusion of weakly constrained nanoprobe in biological environments are greatly needed. Such approaches can improve our understanding of disease pathogenesis and drug delivery.

Current techniques for studying nanoparticle diffusion in biological samples include multiple-particle tracking (MPT) and fluorescence recovery after photobleaching (FRAP), which have been used to characterize the nanostructure of mucus (8) and ECM of tumors (9). The advantage of MPT is that it elucidates heterogeneous nanostructural properties encountered by individual fluorescent nanoparticles. However, MPT requires con-

Significance

Many diseases are characterized by nanostructural changes in connective fibers and soluble proteins, which can indicate or drive disease progression. Noninvasive methods sensitive to nanotopological changes in 3D tissue models can elucidate biophysical changes associated with disease progression. Nanoparticles probe their environment via their diffusion, which is impacted by the size and connectivity of pores into which they freely diffuse. Here, we show that optical coherence tomography provides depth-resolved imaging of gold nanorods (GNRs) to infer local biological nanotopology. We demonstrate the broad potential of this method by sensing changes in diffusion of GNRs in 3D models of mammary ECM and pulmonary mucus.

Author contributions: R.K.C., R.L.B., W.-C.W., D.B.H., B.B., P.C.-H., M.A.T., J.B.T., and A.L.O. designed research; R.K.C., R.L.B., W.-C.W., P.C.-H., and A.L.O. performed research; W.-C.W., D.B.H., B.B., and J.B.T. contributed new reagents/analytic tools; R.K.C., R.L.B., P.C.-H., M.A.T., and A.L.O. analyzed data; and R.K.C. and A.L.O. wrote the paper.

The authors declare no conflict of interest.

This article is a PNAS Direct Submission. C.Y. is a guest editor invited by the Editorial Board.

¹Present address: Howard Hughes Medical Institute, Janelia Farm Research Campus, Ashburn, VA 20147.

²To whom correspondence should be addressed. Email: aold@physics.unc.edu.

This article contains supporting information online at www.pnas.org/lookup/suppl/doi:10.1073/pnas.1409321111/-DCSupplemental.

ment. Current passive rheological methods typically use micro-particles that are highly constrained ($R_H \gg \xi$), and the bulk viscoelasticity is obtained from the measured particle dynamics. In contrast, the GNRs used in this study ($R_H \sim 19\text{--}24\text{ nm}$) are typically on the same size scale as ξ , presenting an appealing avenue to understand nanotopology that is otherwise not elucidated by bulk viscoelasticity measurements.

Previously, we validated that OCT measurements of the rotational diffusion (D_R) of GNRs in Newtonian (molecular) fluids are consistent with a combination of existing models for Stokes drag on cylinders, light scattering from plasmonic rods, and the Stokes–Einstein relation (34), and that D_R can be accurately depth-resolved via coherence gating. Here, we extend this method to measure GNR diffusion in controlled, non-Newtonian (macromolecular) fluids of polyethylene oxide (PEO), noting that there are no readily available models to describe anisotropic probe diffusion in the $R_H \sim \xi$ regime. Thus, these measurements provide a framework to understand subsequent experiments below in complex biological media.

In contrast to our previous study of molecular fluids, here, the molecular solvent (water) is kept constant while the concentration of PEO of fixed molecular weight (1 MDa) is increased above c^* . At c^* , the correlation length ξ is estimated to be 68 nm and to decrease monotonically as the concentration increases (35). Importantly, we found that GNRs in PEO solutions exhibited isotropic autocorrelations that were well described by a single exponential decay at concentrations up to $10c^*$ (SI Text), which was used to unambiguously define D_T over the timescale of the measurement. This is in contrast to what is observed in the strongly constrained regime ($c \gg c^*$), where deviations from a single exponential are observed due to the polymer viscoelasticity (2).

As shown in Fig. 1, we observed that the GNRs are weakly constrained by PEO in the semidilute concentration regime for $R_H/\xi < 2.2$ (i.e., D_T is slowed down by less than a factor of 10 compared with that in the solvent). However, at sufficiently large concentrations such that $R_H/\xi > 2.2$, translational diffusion of GNRs is significantly hindered (i.e., D_T is slowed down by a factor of ~ 100 or more compared with that in pure solvent). Here, we define “weakly constrained” as the regime in which $0.1 \times D_{T,\text{solvent}} < D_T < D_{T,\text{solvent}}$. Within this weakly constrained regime, we found that the D_T of GNRs is sensitive to changes in ξ of the controlled PEO solutions with a power law of ~ 1 . This range of D_T provides a baseline to understand similar obstructed and yet weakly constrained diffusion that GNRs undergo as they percolate through networks, meshes, and pores in the following studies in complex biological fluids and soft solids.

Diffusion of GNRs in *Vitro* ECM Models Is Sensitive to Collagen Concentration and Stromal Cell Concentration. The mammary gland *in vivo* consists of epithelial tissue that forms the mammary ducts; these are embedded in a complex, 3D network comprised of ECM produced and maintained predominantly by stromal fibroblasts. ECM provides structural scaffolding as well as biochemical and biomechanical contextual information to signal appropriate cellular responses (36). Three-dimensional tissue culture models composed of gelatinous proteins, such as collagen I and Matrigel, have been successfully used as surrogate models to mimic the structure and function of the ECM in controlled biological studies (37–39), and have been shown to recapitulate various aspects of *in vivo* tissue behavior (40). Previous studies in the context of drug delivery have highlighted the role of ECM pores for the delivery of nanoscale probes (41, 42).

To elucidate the effect of ECM concentration on GNR diffusion, GNRs ($R_H \sim 24\text{ nm}$) were topically added to 1–3 mg/mL collagen I ECM models. Collagen I gel pore sizes have been estimated to range from ~ 100 to 500 nm at concentrations from 20 to 2 mg/mL, respectively (42). Based on the R_H of GNRs relative to the size of the collagen pores, GNRs are expected to

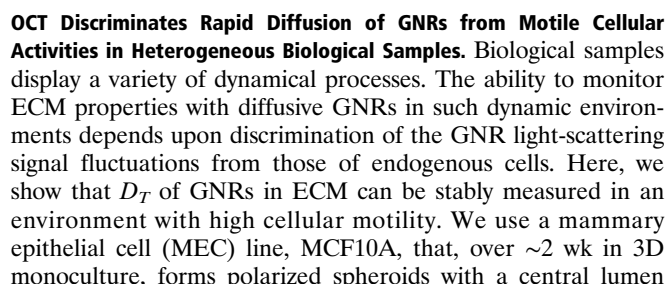
be weakly constrained within the ECM interstitial space. An increased collagen I concentration corresponds to decreased pore size and also an increase in unassembled collagen I in the interstitial space (42). On the bulk scale, increased collagen I concentration is observed to make the gels palpably stiffer (increased elastic modulus).

Collagen I ECM imaged with OCT after overnight topical addition of GNRs revealed strong and spatially homogeneous *HH* (copolarized) and *HV* (cross-polarized) contrast compared with control gel, suggesting a homogeneous distribution of GNRs within the gels. Fig. 2A shows the isotropic autocorrelations, $g^{(1)}_{\text{ISO}}(\tau)$, which portray a decrease in D_T as the concentration of collagen I increases (see SI Text for details). As a comparison, D_T was measured in the solvent alone, which fills the interstitial space of the collagen I gels. The data suggest that the translational motion of the GNRs in the interstitial space of the collagen I gels is slower than that in the solvent, which can be attributed to the increased obstructions presented by the ECM matrix. Importantly, in this weakly constrained regime, GNR diffusion is observed to be sensitive to collagen I concentration while also maintaining sufficient diffusivity for overnight topical application. Using GNRs as minimally invasive diffusion probes with OCT imaging thus offers the possibility to longitudinally monitor ECM remodeling processes, which are ubiquitous in pathogenesis and disease progression.

Toward this end, we then studied the response of GNR diffusion within a mammary tissue model containing reduction mamoplasty fibroblasts (RMFs) expressing green fluorescent protein (GFP). Fibroblasts are the principal cellular components of connective tissues, and act to maintain and modify ECM by adhering and applying tension to ECM fibers (43), depositing collagen [as during wound healing (44)], and even enzymatically degrading ECM [as during tumorigenesis (45)]. To understand nanoscale changes to the ECM pores brought about by fibroblasts, GFP-modified RMFs were seeded in collagen I:Matrigel at varying concentrations (100–500 cells per μL) and maintained for 48–96 h before overnight topical administration of GNRs. Because fibroblasts predominantly scatter copolarized light, *HV* OCT was used to identify regions of GNRs (i.e., high *HV* signal) from fibroblasts (i.e., apparent voids in *HV* images) (Fig. 2B). Thresholding (*Materials and Methods*) was used to ensure that diffusion analysis was only performed in regions of ECM containing GNRs and devoid of RMFs. Fluorescence images of the cultures immediately before GNR administration (Fig. 2C) verified that there was a monotonically increasing cell density with both incubation time and cell seeding density.

Measurements of D_T of GNRs within the 3D tissue models are summarized in Fig. 2D. GNRs within the ECM exhibited significantly decreased D_T with increasing RMF cell seed density at each of the incubation times measured, with the exception of the highest seed density of 500 cells per μL at 48 h (see SI Text for details). At 500 cells per μL , the high cell densities (as evidenced in Fig. 2C) may have caused increased competition for media serum and/or cell death to partially reverse the observed trend. However, for cell seed densities up to 300 per μL , at each of the time points there was a reduction in D_T with cell seed concentration. Two additional experiments were conducted to demonstrate the reproducibility of this trend (see SI Text for details). In those experiments, statistically significant reductions in D_T with increasing RMF cell seed density were evident at 72 and 96 h, but not at the earliest time point of 48 h. This suggests slower cell growth and/or smaller seed densities (within cell-counting error) at earlier time points. Importantly, D_T decreased significantly with increasing seed density at later time points in all three experiments, reinforcing our conclusion that GNRs sense ECM changes as fibroblasts grow.

The reduction in D_T of GNRs with fibroblast concentration may be explained by fibroblast strain stiffening of the ECM and/or additional collagen deposition. Qualitative observations of the



that recapitulates many in vivo features of mammary ductal architecture (37, 46). We have previously demonstrated that OCT provides excellent visualization of MEC spheroids (47), whereas MECs themselves cause detectable light-scattering fluctuations due to their motility (48).

OCT imaging of GNRs typically added to a 3D culture reveals a region of negative contrast in HV due to the exclusion of GNRs from the spheroid formed by MCF10A cells (Fig. 3A). Due to strong copolarized scattering from the spheroid, its presence is masked in HH OCT against a background of highly scattering GNRs in the ECM. Thus, the OCT B-mode images (B mode: depth scans acquired across multiple transverse locations, i.e., x - z scans) show the presence of GNRs in the ECM and the lack of GNRs in the spheroid. Additional information on the time-scales of GNR diffusion and cellular motility are evident from M-mode OCT imaging (M mode: temporal depth scans acquired at one transverse location, i.e., z - t scans). Both HH and HV M-mode data reveal increasingly rapid signal fluctuations in the ECM (shorter horizontal streaks in the M-mode intensity images) compared with those at the location of the MEC spheroid (longer horizontal streaks in the M-mode intensity images) (Fig. 3B). Extraction of the $1/e$ decay constants from the HH and HV autocorrelations, τ_{HH} and τ_{HV} , allow us to quantify the timescales of these fluctuations.

We find that the ECM regions containing diffusing GNRs exhibited characteristically rapid decays, and in particular, that

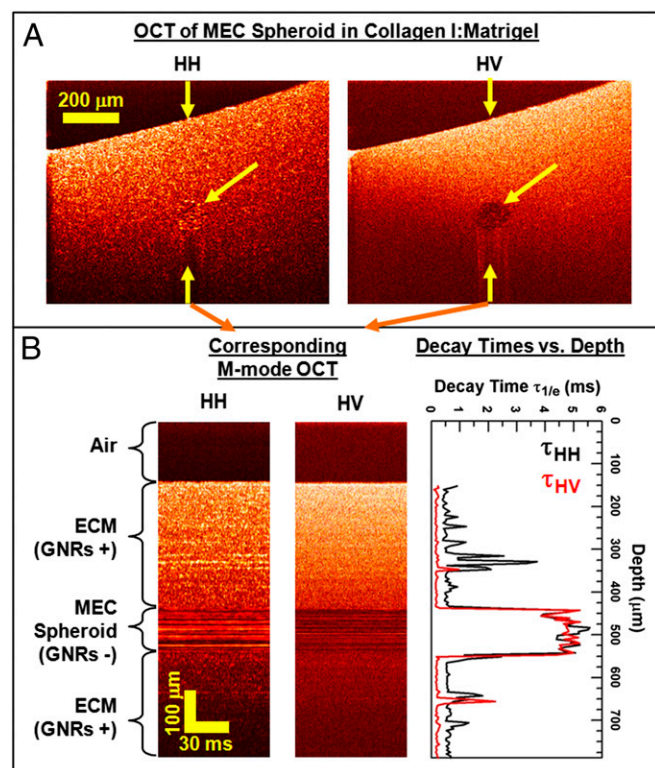


Fig. 3. GNRs typically added to collagen I:Matrigel ECM with a spheroid formed by mammary epithelial cells (MCF10A). (A) Copolarized (HH) and cross-polarized (HV) B-mode images of collagen I:Matrigel ECM show strong scattering from GNRs in the ECM and an absence of GNRs in the spheroid (indicated by arrows). (B) M-mode OCT obtained from the central A-line from images in A (only 75 ms of the 1.2 s of data are shown), and the corresponding depth-resolved τ_{HH} and τ_{HV} are shown. In regions with diffusing GNRs, $\tau_{HV} < \tau_{HH}$ due to the faster decay mode associated with GNR rotation. In the spheroid, $\tau_{HH} \sim \tau_{HV}$ with values that are characteristically larger than those from GNRs in the ECM.

the cross-polarized decay mode is much faster than the copolarized mode ($\tau_{HV} < \tau_{HH}$). In contrast, the MEC spheroid region exhibits comparatively longer decays that are more isotropic ($\tau_{HH} \sim \tau_{HV}$). This can be understood by considering the difference in light-scattering properties of the plasmon-resonant GNRs and the cells in the MEC spheroids. GNRs depict strong polarization-dependent scattering due to plasmon resonance, scattering light into both the copolarized and cross-polarized channels, with rotational diffusion dominating the cross-polarized mode (SI Text). In comparison, cells are not plasmon resonant and are not strongly optically anisotropic; although some tissues exhibit birefringence, we observe that MEC spheroids exhibit little HV contrast. At the same time, larger cellular features (which cause refractive index inhomogeneities on the size scale of the wavelength λ) will tend to dominate the HH light-scattering signal from cells; these larger features experience larger hydrodynamic drag than nanosized objects and concomitantly slower motions (even considering the added energy from ATP metabolism). All of these expectations are consistent with our observations that there are slower and more equal ($\tau_{HH} \sim \tau_{HV}$) decay modes in the cells compared with GNRs.

In Fig. 3B, the depth-resolved τ_{HH} exhibits a region above the spheroid (z of $\sim 320 \mu\text{m}$) where it is longer compared with the surrounding ECM, whereas τ_{HV} remains small; this feature implies that the scattering in this region is dominantly from the diffusing GNRs. This may evidence some heterogeneity in the ECM structure and/or a nearby MEC spheroid out-of-plane relative to the B-mode section. Within the rest of the ECM, D_T of the GNRs was computed to be $3.2 \pm 0.4 \mu\text{m}^2/\text{s}$, in a similar range as that observed in the collagen I:Matrigel ECM for the RMF study. Thus, OCT imaging of diffusive GNRs can reveal heterogeneous ECM properties, such as that caused by remodeling, while exhibiting characteristic decay modes that are distinguishable from endogenous motile activities of cells.

Diffusion of GNRs in Airway Mucus Is Sensitive to Physiologically Relevant Changes in Mucus Concentration. Mucociliary clearance is a vital respiratory defense mechanism that involves trapping inhaled pathogens, toxins, and particulates within the mucus layer lining the airway epithelium and a continuous clearance of mucus by rhythmic beating of cilia in the periciliary layer (PCL) of the epithelium (49). Normal mucociliary clearance is disrupted in respiratory diseases such as cystic fibrosis and chronic obstructive pulmonary disease, which results in more viscous and thicker-layered mucus due to reduced solvent (in cystic fibrosis) or increased mucin content (in chronic obstructive pulmonary disease). To noninvasively image these dynamic processes within the respiratory epithelium, relevant metrics such as mucus flow, mucus layer thickness, ciliary beat frequency, and PCL thickness have been investigated using OCT (50, 51). To complement such efforts, additional information about the mucus viscosity (and associated mucin content) using diffusive, muco-inert GNRs with OCT can provide key biophysical data to understand the mechanism of mucociliary clearance and its breakdown in disease. It can also provide insight in devising mucus-penetrating particles for efficient drug delivery.

Mucus used in this report was derived from well-differentiated in vitro hBE cultures maintained at an air-liquid interface (ALI) (49, 52). Because increased mucus concentration beyond the normal range [$\sim 2\%$ (wt/wt) solid] (49) has previously been correlated with the pathogenesis of airway disease (31, 53), the concentration of airway mucus was explored from the physiologically normal to diseased range [1.5 – 3.5% (wt/wt) solid]. PEGylated GNRs were diffused in the mucus samples and M-mode OCT imaging was performed to extract the diffusion coefficients of the GNRs. The resulting isotropic autocorrelations are well described by a single exponential decay, and are separated at varying mucus concentrations (Fig. 4A). The corresponding D_T of GNRs is observed to monotonically decrease with increasing

mucus concentration over the measured range. Compared with the solvent ($1\times$ PBS), the measured D_T of GNRs in the mucus samples are slowed less than 10-fold, demonstrating that the GNRs are weakly constrained in the mucus mesh. This suggests that mucus, despite being a viscoelastic gel in bulk, behaves as a viscous fluid at the length scale of the GNRs with the mucus macromolecules presenting intermittent obstruction to the diffusion of GNRs. Additionally, this implies that GNRs with a non-adherent 1-kDa PEG surface coating are able to rapidly percolate through the mucus mesh that otherwise efficiently traps a majority of exogenous particles, which corroborates the selective permeability of mucus based on the size of the penetrating particles (54).

OCT Imaging of GNRs in Mucus over an ALI Culture Reveals Diffusion in Mucus and Exclusion of GNRs in the PCL. ALI cultures recapitulate features of human airway epithelium including cell polarization,

formation of a contiguous epithelium, active exclusion of liquid from the apical surface, mucus secretion and accumulation, and coordination of ciliary beating that results in effective mucus transport (52). Here, we use ALI cultures to demonstrate that GNR diffusion in mucus can be accurately measured in an actively transporting system, while elucidating the ability to depth-resolve properties within the mucus layer. GNRs were diffused in mucus at 2.5% (wt/wt) solids and deposited over a transporting ALI culture. The rate of mucus transport on similar samples has been estimated to be $\sim 20\ \mu\text{m/s}$ (50). B-mode images revealed strong GNR contrast in both HH and HV , whereas contrast in HH only that was relatively weaker was observed from the hBE cell layer (Fig. 4B). The normalized cross-polarized (CP) image, a method previously developed for GNR differentiation in a 3D tissue model (48), clearly differentiates regions containing GNRs (high CP) compared with cells (low CP) and background noise

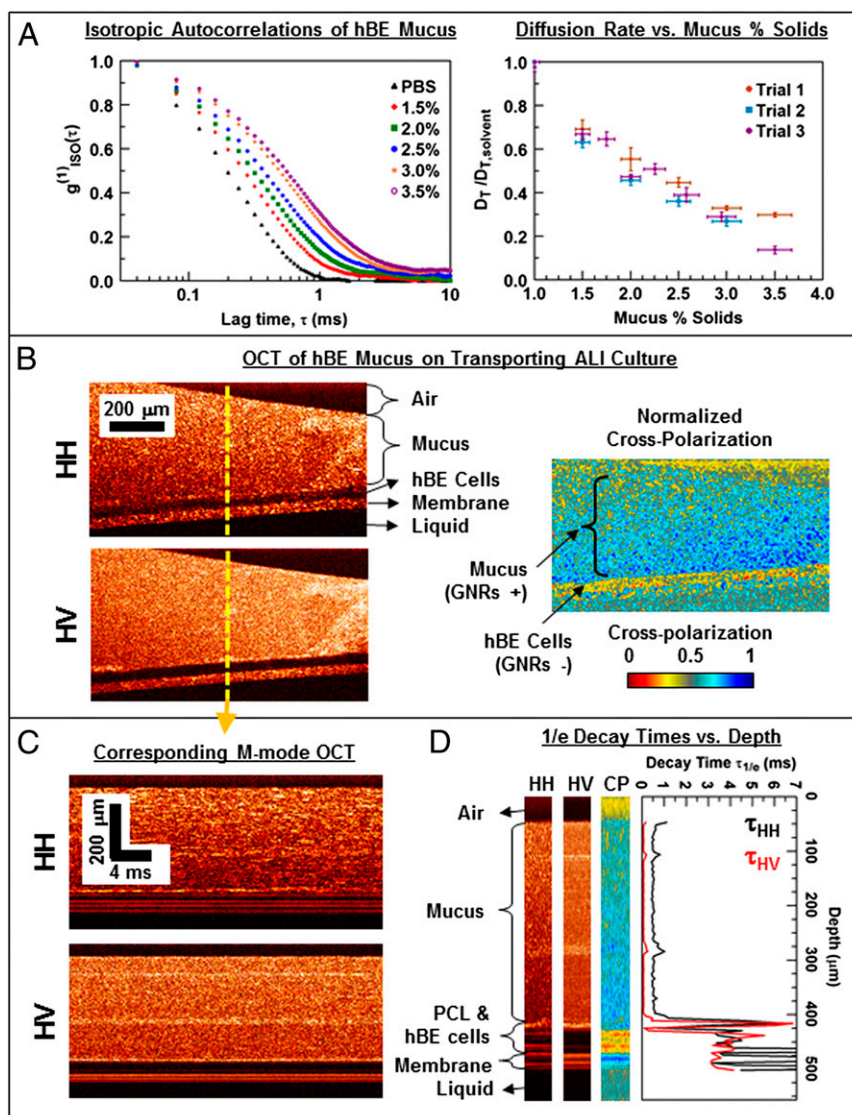


Fig. 4. GNR diffusion in stationary mucus (A) and in actively transporting hBE mucus in an ALI culture (B–D). (A) GNR diffusion in varying mucus percentage solids (where the solvent is $1\times$ PBS at 1% solids). (Left) Representative isotropic autocorrelations. (Right) Corresponding relative diffusion rates $D_T/D_{T,\text{solvent}}$ ($n \geq 6$; average and SD; three independent trials plotted). GNR diffusion is significantly hindered as the mucus solids concentration increases. (B) Representative HH , HV , and CP OCT images of mucus [2.5% (wt/wt) solids] with GNRs on a transporting ALI culture. A layer devoid of GNRs corresponding to hBE cells exhibits low cross-polarization in comparison with GNRs within the mucus layer. (C) A portion of the M-mode OCT data corresponding to the central A-lines of B illustrates more rapid fluctuations in HV compared with HH . (D) Depth-resolved τ_{HH} and τ_{HV} corresponding to C discriminates diffusing GNRs within the mucus from slower motile activities in the PCL and hBE cells. A portion of the HH , HV , and CP M-mode images are shown for comparison of each layer position with the decay rates.

(neutral $CP \sim 0.5$). GNRs appear to be excluded from the apparent hBE cell layer, with an exclusion layer of $\sim 45\text{-}\mu\text{m}$ thickness that is consistent with the typical range of thicknesses of native, healthy bronchi (55).

This interpretation is further corroborated by the temporal data (Fig. 4 C and D). A region of diffusive GNRs is evident by a short τ_{HV} and a comparatively longer τ_{HH} , which appears from the top surface down to $\sim 400\text{-}\mu\text{m}$ depth. In contrast, endogenous light-scattering fluctuations from ciliary activity within the PCL and motility within hBE cells are indicated by longer and nearly equal τ_{HH} and τ_{HV} . Time constants within the stationary membrane supporting the cells become even larger. GNRs in the transporting mucus exhibited D_T of $2.9 \pm 0.3 \mu\text{m}^2/\text{s}$ compared with $D_{T,\text{solvent}}$ of $8.3 \pm 0.4 \mu\text{m}^2/\text{s}$. Importantly, the relative diffusion, $D_T/D_{T,\text{solvent}} = 0.35 \pm 0.04$, is consistent with measurements in stationary mucus at 2.5% (wt/wt) solids (Fig. 4A). The predominantly transverse flow of the mucus thus did not significantly affect the D_T of GNRs measured over the transporting ALI culture, which can be explained by the fact that the mucus traverses a very short distance ($<20\text{ nm}$) over the GNR decay time ($\tau_{1/e} < 1\text{ ms}$) in comparison with the focal spot size used in the OCT system ($12\text{ }\mu\text{m}$).

Interestingly, τ_{HH} and τ_{HV} are relatively constant over most of the mucus layer. Slight increases are noted at depths of ~ 100 and $290\text{ }\mu\text{m}$, which exhibit corresponding bright regions in the OCT images; these may be inhomogeneities in the mucus itself. However, at $\sim 420\text{ }\mu\text{m}$, a large peak in τ_{HH} and τ_{HV} appears at a depth slightly above the apparent hBE region (i.e., above the region exhibiting characteristically low CP). Because the peak appears isotropic ($\tau_{HH} \sim \tau_{HV}$), it is unlikely to be caused by freely diffusing GNRs and may be explained by ciliary activity within the PCL, which is known to have a height of $\sim 5\text{--}10\text{ }\mu\text{m}$ (8, 50). Below $\sim 430\text{ }\mu\text{m}$, the decay constants settle to relatively large and isotropic values within the apparent hBE region, which corresponds to the longer timescale of hBE activity relative to the GNR diffusion. Although the mucus layer used in this study was unusually thick to validate the ability for OCT to penetrate a thick, disease-like state of the epithelium, future studies as a function of mucus thickness may elucidate depth-resolved changes in mucus properties near the PCL, such as shear thinning due to shear forces applied by cilia during transport.

The measurements suggest that GNRs at all depths in the mucus probe the solvent within the mucus mesh with intermittent obstruction from mucin strands, trapped debris, and other constituent macromolecules in mucus, with insignificant perturbation from mucociliary transport within the timescale of the measurement. The use of GNRs in OCT imaging of transporting mucus thus not only simultaneously probes the diffusion of GNRs and slower cellular activities but also elucidates the defensive role the epithelium plays in excluding nanoscale particles. Moreover, the diffusion of GNRs in mucus has implications in understanding the semipermeable nature of mucus in trapping or allowing passage of exogenous particles, which can supplement current efforts in designing efficient mucus-penetrating particles (8, 56, 57).

Conclusion

We have demonstrated the utility of OCT to noninvasively monitor the diffusion of GNRs as they navigate the nanotopology of complex biological fluids and soft solids. The optical tunability and polarization-sensitive scattering of GNRs allows discrimination of their light-scattering signals from those of neighboring cells. In controlled, semidilute polymer solutions, we identified a regime of weakly constrained GNRs that provided a foundation for understanding similar obstructed diffusion in interstitial spaces and pores in complex biological fluids and soft solids.

In soft solids, our results suggested that GNRs were diffusive and weakly constrained in the interstitial space of ECM composed of pure collagen or collagen and Matrigel. Their diffusion

was sensitive to ECM concentration, corresponding to a decrease in pore sizes between the ECM fibers and an increase in unassembled ECM fibers in the interstitial space. GNR diffusion was also sensitive to stromal cell density and culture time, demonstrating the ability to monitor ECM-remodeling processes with this technique. Importantly, GNRs were delivered topically into 3D tissue models, a delivery method that is minimally invasive to the biological system, whereas OCT provided excellent visualization and depth penetration in the optically thick system, which will be favorable for longitudinal studies of disease progression. At the same time, light-scattering fluctuation signals from GNRs were clearly distinguishable from those of cells based on the unique anisotropic and plasmon-resonant characteristics of the GNRs, whereas PEGylation of GNRs prevented significant adherence to ECM proteins or cellular uptake. These features enable a platform for monitoring tissue-remodeling processes such as those related to carcinogenesis.

In biological fluids, it was found that the diffusion of GNRs was sensitive to in vitro hBE mucus for concentrations ranging from physiologically normal to diseased. The muco-inert PEG coating on the GNRs was observed to minimize trapping, as GNRs exhibited weakly constrained diffusion at all mucus concentrations studied. At the same time, D_T measurements of GNRs were stable in actively transporting mucus; taken in combination with the high permeability of GNRs, which is favorable for topical delivery, these features suggest that this method has translational potential for in vivo studies of mucus mechanical properties, and may enable real-time monitoring of mucus-thinning therapies used in cystic fibrosis and chronic obstructive pulmonary disease. The ability for OCT to monitor the diffusion and penetration of GNRs into thick pulmonary mucus may also be favorable for studying nanoparticle-based drug delivery across the mucus barrier.

As an imaging technology, the study of diffusion with OCT is only in its infancy. The use of GNRs demonstrated here offers a highly controlled platform to understand biological nanotopology, whereas new nanoparticle designs or endogenous particle-imaging targets may offer further insights at different size and timescales within viscoelastic media. These methods will also benefit from further development of models to describe anisotropic probe diffusion in complex media. In the field of biomedicine, the truly broad-based technique described here can be immediately applied to pursuits in understanding disease pathogenesis, progression, and treatment.

Materials and Methods

GNR Synthesis and Characterization. GNRs were synthesized following a procedure that some of the authors recently reported (58), which involves stabilization by cetyltrimethylammonium bromide. Subsequent PEGylation of GNRs was performed, using poly(ethylene glycol) methyl ether thiol (Sigma-Aldrich) of 1-kDa molecular weight to avoid adherence with mucus or ECM proteins. Transmission electron microscopy (TEM) was performed and the sizes of $n = 99$ GNRs were measured for each batch, which were $83 \pm 7 \times 22 \pm 3\text{ nm}$ (batch 1) and $62 \pm 10 \times 18 \pm 4\text{ nm}$ (batch 2). The PEG coating thickness was estimated to be 0.48 nm based on TEM measurements of the minimum spacing between GNRs, divided by 2. The hydrodynamic radius R_H of each batch was defined as the R_H of a sphere of equivalent D_T , by equating D_T for a sphere to that for cylinders (59), resulting in the following expression:

$$R_H = \frac{L}{2(\ln(L/w) + 0.312 + 0.565(w/L) - 0.100(w/L)^2)},$$

where L and w are the GNR length and width, respectively, after accounting for the PEG coating thickness. This resulted in $R_H = 24 \pm 2$ and $19 \pm 3\text{ nm}$ for batches 1 and 2, respectively. All studies were performed with GNRs at a final concentration between 6.8×10^7 and 2.4×10^8 GNRs per μL , corresponding to $\sim 14\text{--}68$ GNRs per coherence volume, which is sufficiently small to avoid GNR–GNR collisions over the decay time of the fluctuations.

OCT System. OCT was performed using a custom, ultrahigh-resolution, spectral-domain optical coherence tomography system (see *SI Text* for details), described in detail previously (34). Briefly, the OCT system light source is a Ti:sapphire laser (Griffin; KMLabs) with 800-nm center wavelength and ~125-nm bandwidth, with 3.5 mW of power directed onto the sample. The system returns air in $3 \times 12 \mu\text{m}$ [axial (z) \times transverse (x)]. A free-space interferometer collects the light backscattered from the sample where the copolarized (HH : incident imaging beam is H and the backscattered beam is H) and the cross-polarized (HV : incident beam is H and the backscattered beam is V) components are separated and directed to a custom spectrometer, where each component is imaged onto separate halves of the same line scan camera (Piranha; Dalsa) operated at an adjustable line rate of 1–25 kHz. The sensitivity was measured to be >90 dB (both HH and HV), and the maximum imaging depth was measured to be 2.08 mm in air. B-mode (x - z) OCT imaging was performed by scanning the beam laterally. M-mode (x - t) OCT was used for diffusion measurements, where the imaging beam temporally probed the same axial line within the sample without lateral scanning. A digital dispersion method (60) is used during reconstruction of the complex-analytic OCT signals, \tilde{S}_{HH} and \tilde{S}_{HV} . The magnitudes S_{HH} , S_{HV} , or the normalized cross-polarization $CP = S_{HV}^2 / (S_{HH}^2 + S_{HV}^2)$ are rendered for display; a 12×12 - μm median filter is used for CP rendering.

Determination of the Diffusion Rate of GNRs from OCT Signals. Using this experimental setup, both D_T and D_R of GNRs can be computed from the complex OCT signals. (See *SI Text* for a review of the theoretical framework.) Because GNRs were in a low-viscosity medium of predominantly water, in comparison with our earlier study in high-viscosity solutions (34), the autocorrelation decay times associated with D_R were too rapid for our OCT line scan camera. Thus, the longer decay times associated with D_T are used exclusively in this paper to define GNR diffusivity.

The D_T of GNRs was evaluated by analyzing the copolarized and cross-polarized complex M-mode OCT signals, $\tilde{S}_{HH}(z, t)$ and $\tilde{S}_{HV}(z, t)$. Fluctuations in the real and imaginary parts of these signals were isolated by subtracting their mean at each z pixel. Autocorrelations of these fluctuations were then evaluated at each z pixel and normalized to obtain $g^{(1)}_{HH}(\tau)$, $g^{(1)}_{HV}(\tau)$, and subsequently $g^{(1)}_{ISO}(\tau)$ (see *SI Text* for details). For D_T measurements, $g^{(1)}_{ISO}(\tau)$ was averaged within depth windows of Δz ranging from 6 to 38 μm . D_T was computed for each window by least-squares fitting of $g^{(1)}_{ISO}(\tau) = e^{-q^2 D_T \tau}$ for τ ranging from Δt (the sampling interval) to the decay constant, $\tau_{1/e}$. The fitted $\tau_{1/e}$ was used to compute $D_T = (q^2 \tau_{1/e})^{-1}$, where $q = 4\pi n / \lambda$, and the refractive index was taken to be $n_{\text{water}} = 1.34$. The average and SD of D_T over all windows ($n \geq 6$) were then reported. For depth-resolved plots of $\tau_{1/e}$ (denoted as τ_{HH} and τ_{HV} , respectively), $g^{(1)}_{HH}(\tau)$ and $g^{(1)}_{HV}(\tau)$ were averaged using a window size of $\Delta z = 4.5 \mu\text{m}$.

The reported diffusion coefficient for an ensemble of GNRs represents an estimate up to a time lag of $\tau_{1/e}$ assuming that viscous drag is the dominant hindrance to diffusion; it thus ignores elastic contributions within that duration. In all of the biological samples reported here, we observed no significant deviation of $g^{(1)}_{ISO}(\tau)$ from that of a single exponential up to $\tau_{1/e}$, whereas the polymer experiments revealed elastic contributions only for excessively small mesh sizes (in the strongly constrained regime), as shown in *SI Text*.

Polymer Solutions. Solutions were prepared in $1 \times$ PBS containing GNRs and 1-MDa PEO (Sigma-Aldrich) with final concentrations varying from 0.13% to 5% (wt/wt) corresponding to correlation lengths varying from 67 to 4 nm, respectively. The correlation length ξ was calculated using $\xi = R_g(c^*/c)^{0.75}$, according to ref. 35, where R_g is the radius of gyration of PEO estimated using an experimentally established dependence (61). Solutions were homogenized by stirring for several days. GNRs from batches 1 and 2 were used with PEO solutions at 0.13–1.25% (wt/wt) and 2.5–5% (wt/wt), respectively, for D_T measurements. $D_{T, \text{solvent}}$ was taken as the theoretical value according to ref. 59.

Three-Dimensional Mammary Cell Cultures. The reduction mammaplasty fibroblast (RMF-GFP) is a stable cell line that constitutively expresses GFP (62). RMF-GFPs were maintained as previously published (28) in RPMI medium. GFP expression was obtained through a lentiviral infection with puromycin as the selection antibiotic. MCF10A is a mammary epithelial cell line (MEC), which was maintained as previously published (47) in DMEM/F12 media. For the collagen study, collagen I (BD Biosciences) at 1–3 mg/mL final concentration was gelled in DMEM/F12 media. For studies with cells, 1:1 collagen I: Matrigel (BD Biosciences) was prepared and seeded with RMF-GFP or MEC as described previously (47), with the final collagen I concentration at 1 mg/mL. RMF-GFP 3D cultures were seeded at three different concentrations (100, 300, and 500 cells per μL) and were incubated for 48, 72, and 96 h. MEC 3D cultures were seeded at 30 cells per μL and were incubated for 2 wk. All 3D cultures were maintained at 37°C and 5% CO_2 with daily media (RPMI for RMF-GFP cultures and DMEM/F12 for MEC cultures) changes until imaging.

One day before imaging, GNRs from batch 1 were dispersed into collagen I samples and RMF 3D cultures, whereas GNRs from batch 2 were dispersed into MEC 3D cultures, by exchanging 200 μL of cell culture media containing GNRs with the existing cell media. To accurately measure D_T in the RMF cultures, regions containing RMFs were removed from the analysis by the merit of their minimal signal in cross-polarization (HV) OCT. Specifically, an automated routine segmented the region of interest (ROI) as that from the top surface of the sample down to the first pixel in HV with intensity less than a threshold. This resulted in the ROI of each sample to always range from the surface of the sample to a depth for which cellular structure was detected.

Statistical analysis to compare D_T of GNRs between different datasets was performed as follows. For the collagen study, a homoscedastic, two-tailed t test was chosen based on the assumption of equal variance of GNR diffusion in all samples. For the RMF study, a heteroscedastic, two-tailed t test was chosen to compare cell densities based on the assumption of different variance of data. In both studies, significance was considered for values of $P < 0.0083$ after Bonferroni correction for multiple comparisons.

Airway Mucus and ALI Bronchi-Epithelial Cell Cultures. Primary, normal hBE cells were harvested from excess surgical tissue procured by the University of North Carolina (UNC) Tissue Core Facility and then cultured on a 0.4-mm pore-sized Millicell (Millipore) coated with collagen and maintained in ALI media (UNC Tissue Core) as described in ref. 63. After 6 wk, hBE cells were confluent with fully developed cilia and the ability to transport mucus for transporting ALI studies. Mucus was harvested from these cultures as previously described (31, 64, 65). Once cultures reached confluence, washings from >100 cultures were pooled and then concentrated against Spectra/Gel. Mucus specimens were then dialyzed against PBS to ensure isotonicity as previously described (31, 64). D_T measurements were obtained of GNRs (batch 1) combined with hBE mucus at varying dilutions in $1 \times$ PBS. Subsequently, one batch of hBE mucus at 2.5% (wt/wt) solids with GNRs was introduced onto the top of a transporting ALI culture for both D_T measurements and B-mode OCT imaging. $D_{T, \text{solvent}}$ was taken as the experimental value in $1 \times$ PBS.

ACKNOWLEDGMENTS. We acknowledge the assistance of Timothy O'Brien in the Computer Integrated Systems for Microscopy and Manipulation, and Jason M. Cooper in Biomedical Engineering, both at the University of North Carolina at Chapel Hill. This work was supported by funds from the National Institutes of Health including Grants R21HL111968 (to A.L.O.) and R21CA179204 (to A.L.O.), pilot funds to A.L.O. and M.A.T. from Grant U54CA119343 (Carolina Center of Cancer Nanotechnology Excellence), funds to P.C.-H. and M.A.T. from Grant U01ES019472 (to M.A.T.), funds to D.B.H. and B.B. from Grant P01HL108808 (R. C. Boucher), funds from the National Science Foundation including Grants DMR-1056653 (to J.B.T.) and DMS-110281 (to D.B.H.), and funds from the Cystic Fibrosis Foundation including Grant BUTTON07XX0.

- Bansil R, Stanley E, LaMont JT (1995) Mucin biophysics. *Annu Rev Physiol* 57(1): 635–657.
- Mason TG, Weitz DA (1995) Optical measurements of frequency-dependent linear viscoelastic moduli of complex fluids. *Phys Rev Lett* 74(7):1250–1253.
- Cheng Z, Mason TG (2003) Rotational diffusion microrheology. *Phys Rev Lett* 90(1): 018304.
- Dasgupta BR, Tee SY, Crocker JC, Frisken BJ, Weitz DA (2002) Microrheology of polyethylene oxide using diffusing wave spectroscopy and single scattering. *Phys Rev E Stat Nonlin Soft Matter Phys* 65(5):051505.
- Mason T, Ganesan K, van Zanten J, Wirtz D, Kuo S (1997) Particle tracking microrheology of complex fluids. *Phys Rev Lett* 79(17):3282–3285.
- Kirch J, et al. (2012) Optical tweezers reveal relationship between microstructure and nanoparticle penetration of pulmonary mucus. *Proc Natl Acad Sci USA* 109(45): 18355–18360.
- Guck J, et al. (2005) Optical deformability as an inherent cell marker for testing malignant transformation and metastatic competence. *Biophys J* 88(5):3689–3698.
- Lai SK, Wang Y-Y, Hanes J (2009) Mucus-penetrating nanoparticles for drug and gene delivery to mucosal tissues. *Adv Drug Deliv Rev* 61(2):158–171.
- Netti PA, Berk DA, Swartz MA, Grodzinsky AJ, Jain RK (2000) Role of extracellular matrix assembly in interstitial transport in solid tumors. *Cancer Res* 60(9):2497–2503.
- Link S, El-Sayed MA (1999) Size and temperature dependence of the plasmon absorption of colloidal gold nanoparticles. *J Phys Chem B* 103(21):4212–4217.
- Sönnichsen C, Alivisatos AP (2005) Gold nanorods as novel nonbleaching plasmon-based orientation sensors for polarized single-particle microscopy. *Nano Lett* 5(2): 301–304.
- Huang D, et al. (1991) Optical coherence tomography. *Science* 254(5035):1178–1181.
- Drexler W, Fujimoto JG (2008) *OCT: Technology and Applications* (Springer, Berlin).
- Boas DA, Bizheva KK, Siegel AM (1998) Using dynamic low-coherence interferometry to image Brownian motion within highly scattering media. *Opt Lett* 23(5):319–321.

15. Berne BJ, Pecora R (1976) *Dynamic Light Scattering: With applications to chemistry, biology, and physics* (Dover Publications, New York).
16. Johnson CS, Jr, Gabriel DA (1981) *Laser Light Scattering* (Dover Publications, New York).
17. Pine DJ, Weitz DA, Chaikin PM, Herbolzheimer E (1988) Diffusing wave spectroscopy. *Phys Rev Lett* 60(12):1134–1137.
18. Mason TG, Gang H, Weitz DA (1997) Diffusing-wave-spectroscopy measurements of viscoelasticity of complex fluids. *J Opt Soc Am A Opt Image Sci Vis* 14(1):139–149.
19. Bizheva K, Siegel A, Boas D (1998) Path-length-resolved dynamic light scattering in highly scattering random media: The transition to diffusing wave spectroscopy. *Phys Rev E Stat Phys Plasmas Fluids Relat Interdiscip Topics* 58(6):7664–7667.
20. Wax A, Yang C, Dasari RR, Feld MS (2001) Path-length-resolved dynamic light scattering: Modeling the transition from single to diffusive scattering. *Appl Opt* 40(24):4222–4227.
21. Mason TG, Gang H, Weitz DA (1996) Rheology of complex fluids measured by dynamic light scattering. *J Mol Struct* 383(1–3):81–90.
22. Kalkman J, Sprik R, van Leeuwen TG (2010) Path-length-resolved diffusive particle dynamics in spectral-domain optical coherence tomography. *Phys Rev Lett* 105(19):198302.
23. Lee J, Wu W, Jiang JY, Zhu B, Boas DA (2012) Dynamic light scattering optical coherence tomography. *Opt Express* 20(20):22262–22277.
24. Kim CS, Qi W, Zhang J, Kwon YJ, Chen Z (2013) Imaging and quantifying Brownian motion of micro- and nanoparticles using phase-resolved Doppler variance optical coherence tomography. *J Biomed Opt* 18(3):030504.
25. Popescu G, Dogariu A, Rajagopalan R (2002) Spatially resolved microrheology using localized coherence volumes. *Phys Rev E Stat Nonlin Soft Matter Phys* 65(4):041504.
26. Sharma RC, Papagiannopoulos A, Waigh TA (2008) Optical coherence tomography picorheology of biopolymer solutions. *Appl Phys Lett* 92(17):173903.
27. Chang W-S, Ha JW, Slaughter LS, Link S (2010) Plasmonic nanorod absorbers as orientation sensors. *Proc Natl Acad Sci USA* 107(7):2781–2786.
28. Camp JT, et al. (2011) Interactions with fibroblasts are distinct in basal-like and luminal breast cancers. *Mol Cancer Res* 9(1):3–13.
29. Casbas-Hernandez P, et al. (2013) Role of HGF in epithelial-stromal cell interactions during progression from benign breast disease to ductal carcinoma in situ. *Breast Cancer Res* 15(5):R82.
30. Boucher RC (2001) Pathogenesis of cystic fibrosis airways disease. *Trans Am Clin Climatol Assoc* 112:99–107.
31. Matsui H, et al. (2006) A physical linkage between cystic fibrosis airway surface dehydration and *Pseudomonas aeruginosa* biofilms. *Proc Natl Acad Sci USA* 103(48):18131–18136.
32. Cai L, Panyukov S, Rubinstein M (2011) Mobility of spherical probe objects in polymer liquids. *Macromolecules* 44(19):7853–7863.
33. Rubinstein M, Colby RH (2003) *Polymer Physics* (Oxford Univ Press, New York).
34. Chhetri RK, Kozek KA, Johnston-Peck AC, Tracy JB, Oldenburg AL (2011) Imaging three-dimensional rotational diffusion of plasmon resonant gold nanorods using polarization-sensitive optical coherence tomography. *Phys Rev E Stat Nonlin Soft Matter Phys* 83(4):040903.
35. Cooper EC, Johnson P, Donald AM (1991) Probe diffusion in polymer solutions in the dilute/semi-dilute crossover regime: 1. Poly(ethylene oxide). *Polymer (Guildf)* 32(15):2815–2822.
36. Bissell MJ, Radisky D (2001) Putting tumours in context. *Nat Rev Cancer* 1(1):46–54.
37. Debnath J, Muthuswamy SK, Brugge JS (2003) Morphogenesis and oncogenesis of MCF-10A mammary epithelial acini grown in three-dimensional basement membrane cultures. *Methods* 30(3):256–268.
38. Kenny PA, et al. (2007) The morphologies of breast cancer cell lines in three-dimensional assays correlate with their profiles of gene expression. *Mol Oncol* 1(1):84–96.
39. Johnson KR, Leight JL, Weaver VM (2007) Demystifying the effects of a three-dimensional microenvironment in tissue morphogenesis. *Methods Cell Biol* 83:547–583.
40. Weaver VM, et al. (2002) beta4 integrin-dependent formation of polarized three-dimensional architecture confers resistance to apoptosis in normal and malignant mammary epithelium. *Cancer Cell* 2(3):205–216.
41. Ramanujan S, et al. (2002) Diffusion and convection in collagen gels: Implications for transport in the tumor interstitium. *Biophys J* 83(3):1650–1660.
42. Erikson A, Andersen HN, Naess SN, Sikorski P, Davies C de L (2008) Physical and chemical modifications of collagen gels: Impact on diffusion. *Biopolymers* 89(2):135–143.
43. Desmoulière A, Chaponnier C, Gabbiani G (2005) Tissue repair, contraction, and the myofibroblast. *Wound Repair Regen* 13(1):7–12.
44. Kalluri R, Zeisberg M (2006) Fibroblasts in cancer. *Nat Rev Cancer* 6(5):392–401.
45. Heppner KJ, Matrisian LM, Jensen RA, Rodgers WH (1996) Expression of most matrix metalloproteinase family members in breast cancer represents a tumor-induced host response. *Am J Pathol* 149(1):273–282.
46. Krause S, Maffini MV, Soto AM, Sonnenschein C (2008) A novel 3D in vitro culture model to study stromal-epithelial interactions in the mammary gland. *Tissue Eng Part C Methods* 14(3):261–271.
47. Chhetri RK, Phillips ZF, Troester MA, Oldenburg AL (2012) Longitudinal study of mammary epithelial and fibroblast co-cultures using optical coherence tomography reveals morphological hallmarks of pre-malignancy. *PLoS One* 7(11):e49148.
48. Oldenburg AL, et al. (2013) Motility-, autocorrelation-, and polarization-sensitive optical coherence tomography discriminates cells and gold nanorods within 3D tissue cultures. *Opt Lett* 38(15):2923–2926.
49. Button B, et al. (2012) A periciliary brush promotes the lung health by separating the mucus layer from airway epithelia. *Science* 337(6097):937–941.
50. Oldenburg AL, Chhetri RK, Hill DB, Button B (2012) Monitoring airway mucus flow and ciliary activity with optical coherence tomography. *Biomed Opt Express* 3(9):1978–1992.
51. Liu L, et al. (2013) Method for quantitative study of airway functional microanatomy using micro-optical coherence tomography. *PLoS One* 8(1):e54473.
52. Fulcher ML, Gabriel S, Burns KA, Yankaskas JR, Randell SH (2005) Well-differentiated human airway epithelial cell cultures. *Methods Mol Med* 107:183–206.
53. Mall M, Grubb BR, Harkema JR, O'Neal WK, Boucher RC (2004) Increased airway epithelial Na⁺ absorption produces cystic fibrosis-like lung disease in mice. *Nat Med* 10(5):487–493.
54. Lai SK, Wang Y-Y, Cone R, Wirtz D, Hanes J (2009) Altering mucus rheology to “solidify” human mucus at the nanoscale. *PLoS One* 4(1):e4294.
55. Verkman AS, Song Y, Thiagarajah JR (2003) Role of airway surface liquid and sub-mucosal glands in cystic fibrosis lung disease. *Am J Physiol Cell Physiol* 284(1):C2–C15.
56. Lai SK, et al. (2007) Rapid transport of large polymeric nanoparticles in fresh undiluted human mucus. *Proc Natl Acad Sci USA* 104(5):1482–1487.
57. Schuster BS, Suk JS, Woodworth GF, Hanes J (2013) Nanoparticle diffusion in respiratory mucus from humans without lung disease. *Biomaterials* 34(13):3439–3446.
58. Kozek KA, Kozek KM, Wu W-C, Mishra SR, Tracy JB (2013) Large-scale synthesis of gold nanorods through continuous secondary growth. *Chem Mater* 25(22):4537–4544.
59. Ortega A, Garcia de la Torre J (2003) Hydrodynamic properties of rodlike and disklike particles in dilute solution. *J Chem Phys* 119(18):9914–9919.
60. Oldenburg AL, Chhetri RK (2011) Digital dispersion compensation for ultrabroad-bandwidth single-camera spectral-domain polarization-sensitive OCT. *Proc SPIE* 7889:78891V.
61. Devanand K, Selser JC (1991) Asymptotic behavior and long-range interactions in aqueous solutions of poly(ethylene oxide). *Macromolecules* 24(22):5943–5947.
62. Proia DA, Kuperwasser C (2006) Reconstruction of human mammary tissues in a mouse model. *Nat Protoc* 1(1):206–214.
63. Rubin BK (2007) Mucus structure and properties in cystic fibrosis. *Paediatr Respir Rev* 8(1):4–7.
64. Hill DB, Button B (2012) Establishment of respiratory air-liquid interface cultures and their use in studying mucin production, secretion, and function. *Methods Mol Biol* 842:245–258.
65. Matsui H, et al. (2005) Reduced three-dimensional motility in dehydrated airway mucus prevents neutrophil capture and killing bacteria on airway epithelial surfaces. *J Immunol* 175(2):1090–1099.

Supporting Information

Chhetri et al. 10.1073/pnas.1409321111

SI Text

Framework for Optical Coherence Tomography-Based Measurements of Gold Nanorod Diffusion

Here, we describe a framework for measuring gold nanorod (GNR) diffusion in biological samples via optical coherence tomography (OCT). OCT is a method of low-coherence interferometry in which a broadband light source is used, and the backscattered light from a biological sample is combined with a reference beam (1). In the spectral domain OCT system used in this study, the intensity of the combined beam is measured by a spectrometer (Fig. S1). The resulting spectral interferogram is Fourier transformed to obtain the light-scattering signal from each depth (z) within the sample, where the depth resolution is proportional to the coherence length of the light source (2). To describe stochastic particle motions in this system, we refer to either normalized (g) or unnormalized (G) autocorrelation functions of the light-scattering signals, which are either based on the electric field (first-order), or the intensity (second-order). Because OCT is a heterodyne (mixing) experiment, the heterodyne Siegert relation (1, 2) provides a direct relationship between the second-order autocorrelation $g^{(2)}(\tau)$ of the OCT measurement, and the first-order autocorrelation $g^{(1)}(\tau)$ needed for diffusion measurements:

$$g^{(2)}(\tau) = \text{Re} \left[g^{(1)}(\tau) \right].$$

In this way, the real-valued $g^{(1)}(\tau)$ are evaluated directly from the OCT intensity fluctuations.

Now, consider the polarized light scattering from an ensemble of identical particles undergoing Brownian motion that are sufficiently dilute to avoid particle–particle collisions over the timescale of the measurement. When the particles are optically isotropic, the first-order autocorrelation of the scattered field, $G^{(1)}$, is a function of the translational self-diffusion coefficient of the particles, D_T . In the case of optically anisotropic particles, such as GNRs, $G^{(1)}$ is additionally dependent on the rotational self-diffusion, D_R , of the particles (3, 4):

$$G^{(1)}(\tau) \propto \langle \alpha^*(0)\alpha(\tau) \rangle e^{-q^2 D_T \tau},$$

where the polarizability correlation term $\langle \alpha^*(0)\alpha(\tau) \rangle$ depends upon D_R . As polarized light impinges on GNRs, the magnitude and direction of the induced dipole moment fluctuates as the GNRs continually reorient themselves, giving rise to a fluctuating, elliptically polarized, scattered light field. Here, we apply horizontally polarized light (H) onto the sample and detect the horizontal (H) and vertical (V) polarization components of the backscattered field. This field is measured from a spatially resolved volume (the coherence volume) using OCT, in which there is an ensemble of GNRs that give rise to a collective, fluctuating signal. In copolarized detection (HH , i.e., horizontal field applied and horizontal field detected), the field autocorrelation is given by the following:

$$G_{HH}^{(1)}(\tau) \propto \left(\alpha_o^2 + \frac{4}{45} \beta_o^2 e^{-6D_R \tau} \right) e^{-q^2 D_T \tau}.$$

In cross-polarized detection (HV , i.e., horizontal field applied and vertical field detected), the field autocorrelation is given by the following:

$$G_{HV}^{(1)}(\tau) \propto \frac{1}{15} \beta_o^2 e^{-6D_R \tau} e^{-q^2 D_T \tau},$$

where $\alpha_o = (2\alpha_{\parallel} + \alpha_{\perp})/3$ is the mean polarizability, and $\beta_o = (\alpha_{\parallel} - \alpha_{\perp})$ is the anisotropy. Because GNRs are axisymmetric, their polarizability tensor is described by α_{\parallel} and α_{\perp} , the components along the long and short axes of the GNRs, respectively. The corresponding normalized first-order autocorrelations, $g^{(1)}$, are then given by the following:

$$\begin{aligned} g_{HH}^{(1)}(\tau) &= \left(\frac{45\alpha_o^2}{45\alpha_o^2 + 4\beta_o^2} \right) e^{-q^2 D_T \tau} + \left(\frac{4\beta_o^2}{45\alpha_o^2 + 4\beta_o^2} \right) e^{-6D_R \tau} e^{-q^2 D_T \tau} \\ g_{HV}^{(1)}(\tau) &= e^{-6D_R \tau} e^{-q^2 D_T \tau}. \end{aligned} \quad [\text{S1}]$$

Importantly, at the longitudinal surface plasmon resonance of the GNRs, $\alpha_{\parallel} \gg \alpha_{\perp}$; using previously reported computational methods (3), we estimate that $\alpha_{\parallel}/\alpha_{\perp} \sim 1,600$ for the GNRs in this study. Thus, the mean polarizability α_o and optical anisotropy β_o of GNRs can be approximated as $\alpha_{\parallel}/3$ and α_{\parallel} , respectively. One important consequence of the large optical anisotropy of GNRs is that it gives rise to large contrast in cross-polarized (HV) images, which allows GNRs to be distinguished within biological tissues which are only weakly anisotropic. The other consequence is that the normalized first-order autocorrelations simplify to the following:

$$\begin{aligned} g_{HH}^{(1)}(\tau) &= \left(\frac{5}{9} \right) e^{-q^2 D_T \tau} + \left(\frac{4}{9} \right) e^{-6D_R \tau} e^{-q^2 D_T \tau} \\ g_{HV}^{(1)}(\tau) &= e^{-6D_R \tau} e^{-q^2 D_T \tau}. \end{aligned} \quad [\text{S2}]$$

A linear combination of these autocorrelations isolates the D_T term, which is known as the isotropic autocorrelation, $g_{ISO}^{(1)}$:

$$g_{ISO}^{(1)}(\tau) = \left(\frac{9}{5} \right) g_{HH}^{(1)}(\tau) - \left(\frac{4}{5} \right) g_{HV}^{(1)}(\tau) = e^{-q^2 D_T \tau}. \quad [\text{S3}]$$

Using this expression, we obtain the D_T of an ensemble of GNRs from measurements of $g_{HH}^{(1)}$ and $g_{HV}^{(1)}$. Also, because the GNRs in this study are small compared with the wavelength ($L < \lambda$), the $1/e$ decay time associated with D_T is much longer than D_R [i.e., $6D_R/q^2 D_T$ varies with $(\lambda/L)^2$ and ~ 9 in this study]. Thus, the D_R of an ensemble of GNRs can be obtained using the following approximation:

$$g_{HV}^{(1)}(\tau) \approx e^{-6D_R \tau}. \quad [\text{S4}]$$

Although the GNRs in our study are not perfectly identical, we find that they are sufficiently monodisperse such that the $g_{HV}^{(1)}$ and $g_{ISO}^{(1)}$ are well described by single-exponential decays, which can be thought of as ensemble-averaged measurements.

Importantly, for GNRs, the approximate $1/e$ decay time observed for $g_{HH}^{(1)}(\tau)$ (Eq. S2) is weighted by both D_R and D_T and does not fit a single exponential. In comparison, τ_{HV} (Eq. S4) is dominated by D_R and is therefore significantly shorter. This is in contrast to light-scattering signals from cells, which are described more generally by Eq. S1 with additional fluctuations due to cellular motility. If we consider that cells are not plasmon resonant, cellular features (refractive index heterogeneities) on the order of $L \sim \lambda$ tend to dominate the light-scattering signal. In this

case, the decay mode anisotropy disappears because both τ_{HH} and τ_{HV} depend strongly on D_T . Also, the decay rates from cells

are slower than those of GNRs owing to the larger hydrodynamic sizes of the scatterers.

1. Huang D, et al. (1991) Optical coherence tomography. *Science* 254(5035):1178–1181.
2. Fercher AF, Hitzinger CK, Kamp G, El-Zaiat SY (1995) Measurement of intraocular distances by backscattering spectral interferometry. *Opt Commun* 117(1-2):43–48.

3. Berne BJ, Pecora R (1976) *Dynamic Light Scattering* (Dover Publications, New York).
4. Johnson CS, Jr, Gabriel DA (1981) *Laser Light Scattering* (Dover Publications, New York).

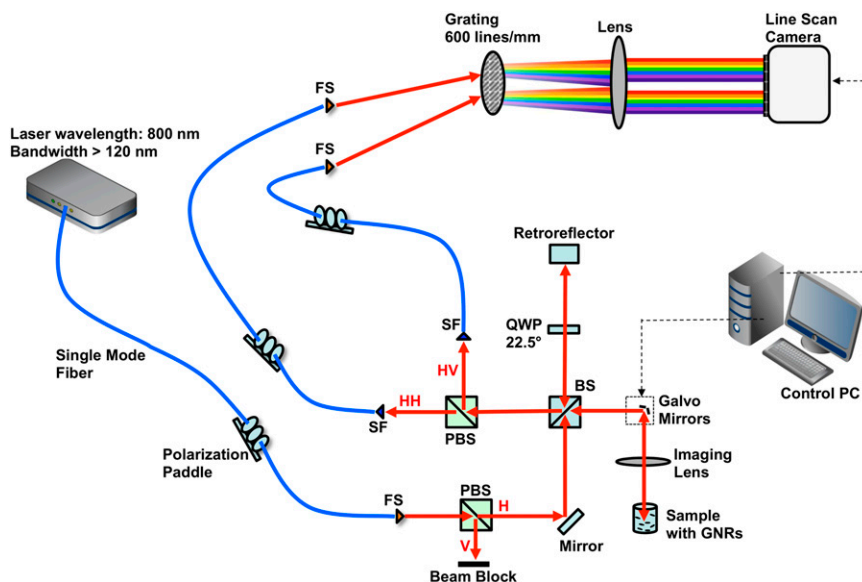


Fig. S1. Schematic of the custom OCT system. Light from a Ti:sapphire laser is guided to a free-space Michelson interferometer, and the polarization-dependent interferograms are detected by a free-space spectrometer. BS, 50–50 nonpolarizing beam splitter; FS, fiber to free-space coupler; HH, copolarized component; HV, cross-polarized component; PBS, 50–50 polarizing beam splitter; QWP, quarter wave plate; SF, free-space to fiber coupler.

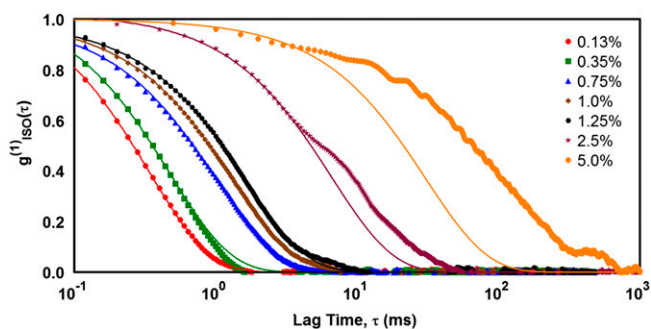


Fig. S2. Inverse exponential fitting to isotropic temporal autocorrelations $[g_{iso}^{(1)}(\tau)]$ of GNRs in 1-MDa PEO at varying concentrations. In the weakly constrained regime [PEO concentration $\leq 1.25\%$ (wt/wt)], $g_{iso}^{(1)}(\tau)$ is well described by an inverse exponential, and thus the diffusion rate of GNRs is well defined within the timescale of the measurement. At higher concentrations, the viscoelasticity of the PEO causes significant deviation of $g_{iso}^{(1)}(\tau)$ from a single exponential. [Fit lines for 2.5% (wt/wt) and 5.0% (wt/wt) are for illustrative purposes only and were performed for $g_{iso}^{(1)}(\tau) > 0.6$ and 0.88, respectively. All other lines were fitted for $g_{iso}^{(1)}(\tau) > 1/e$ as in *Materials and Methods*.]

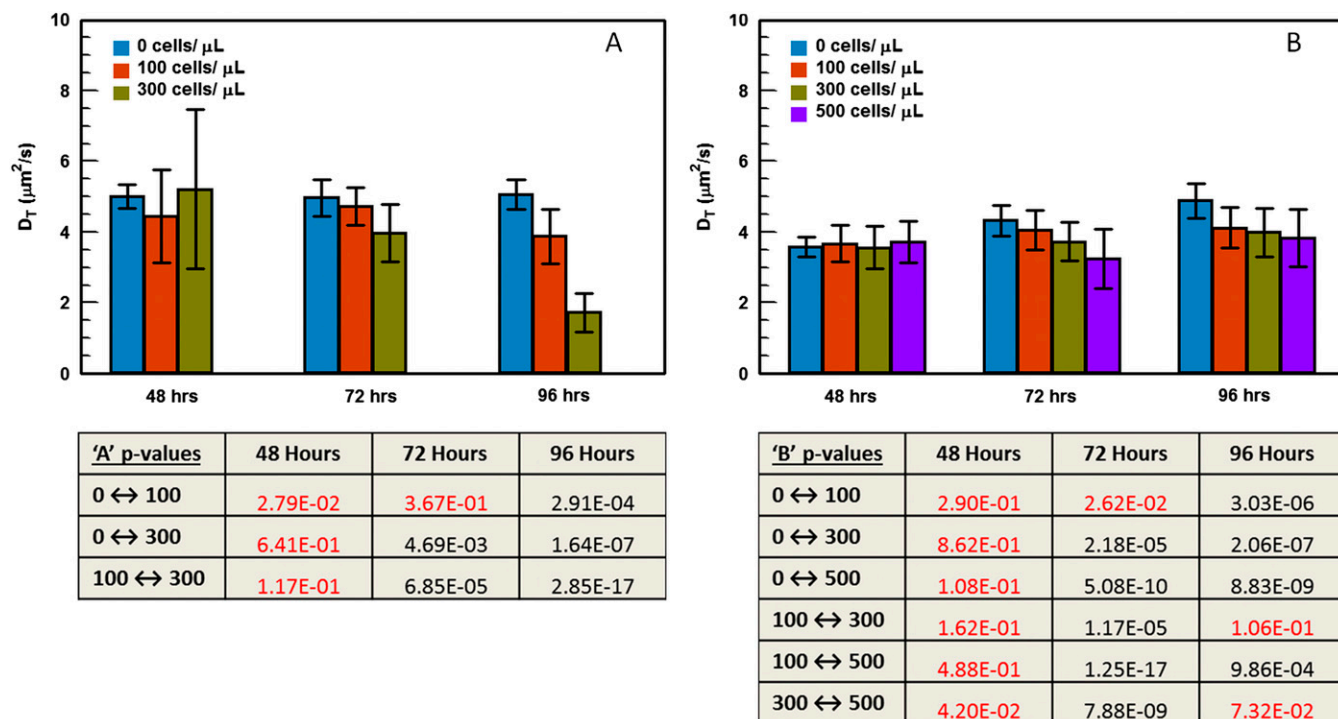


Fig. S3. Diffusion rate of GNRs in 3D cultures for increasing fibroblast density and incubation time. Two additional trials of experiments with fibroblasts were conducted to demonstrate reproducibility of the trend reported in Fig. 2D. (A) Comparison of three seed densities over three separate incubation times (control, $n = 12$; all other, $n = 24-36$; average and SD), with the decrease in diffusion of GNRs for higher cell concentrations becoming more significant as the incubation time increases. (B) Comparison of four seed densities for the three incubation times (control, $n = 12$; all other, $n = 96-156$; average and SD), with decreasing diffusion rates of GNRs for higher cell concentrations evident at the longer two incubation times, 72 and 96 h. P values for D_T measurements comparing different cell seed densities at each incubation time are given in tables corresponding to the fibroblast data reported in each panel.

Table S1. P values for D_T measurements comparing different collagen concentrations, corresponding to the data reported in Fig. 2B

CM represents cell media control. Statistically significant values are displayed in black, and insignificant value is in red.

Statistically significant values are displayed in black, and insignificant value is in red.